

Experimental and Theoretical Explorations on the Buckling Piezoelectric Layer Under Magnetic Excitation

KAYHAN ÇELİK,^{1,3} EROL KURT,¹ and YUNUS UZUN²

1.—Department of Electrical and Electronics Engineering, Technology Faculty, Gazi University, 06500 Beşevler, Ankara, Turkey. 2.—Department of Electrical and Electronics Engineering, Engineering Faculty, Aksaray University, Aksaray, Turkey. 3.—e-mail: kayhancelik1923@gmail.com

In the present study, experimental and theoretical explorations on the buckling features of a wind energy harvester have been performed. The harvester consists of a piezoelectric layer, which has a certain stiffness and voltage conversion rate. A blade rotates on a shaft carrying a magnet and sweeps the tip of the layer causing a serial buckling effect resulting in energy generation. Since the modeling of the buckling under a magnetic strength includes nonlinear terms over displacements, one requires a detailed study on the characteristics of buckling phenomena. It has been proven that the piezoelectric beam having the magnet at its tip can produce regular and chaotic dynamics for different frequencies (i.e. the rotation speed). In addition, there exist a number of quasi-periodic regions on the parameter space. The overall result indicates that the large area of complicated dynamics requires a detailed study in order to stabilize the position and velocity of the layer tip, thereby a much stabilized energy conversion from mechanical to electrical can be obtained. The present survey on the dynamics of the harvester is a new study and is considered as a two-parameter diagram [i.e. the wind speed (frequency) and magnetic strength]. Mainly, single-, double-, triple- and quadruple-type phase space portraits have been observed and the ripples on the maximal and minimal values of the beam velocity have been observed for certain rotation speeds. These results can be used in order to stabilize the harvester in terms of the reduction of total harmonic distortion in the generated waveform.

Key words: Piezoelectric, buckling, power, magnetic field, chaos

INTRODUCTION

Energy demand in the community is forcing researchers to model and implement new and efficient energy harvesting techniques. The harvesting techniques especially aim to cover the power requirements of autonomous sensor nodes, alarm systems, actuators and other micro- or milliwatt consuming devices. While the harvesters enable the enhancement of the lifetimes of the regenerative systems and operations, they can also serve as a unique source without a battery.^{1,2}

Portable and wireless devices such as alarm systems, mobile weather devices and sensors can have longer battery lives, and thereby require less recharging time by applying harvesting mechanisms. Among all harvesting mechanisms, the conversion of mechanical energy from background vibrations into electrical energy via a piezoelectric (PZT) layer has the highest power density.¹⁻³ In recent studies, the PZT systems can have longer lifetime due to the contactless operation with the help of magnetic repelling.^{4,5} However, parallel to the literature, a PZT layer can be very effective when it operates at its own resonance frequency.^{6,7} In that case, the main problem remains the conversion of the surrounding excitation frequencies to the resonance frequency, because a wide-band vibration

character is encountered in nature and these lead to random excitations of the harvester and cause a vital decay in the power generation.

The discussions above take us to a point where the importance of the frequency of the external stress (i.e. mechanical vibration) exists. The reality that the background vibrations lead to a wide-band frequency spectrum motivates us to explore the characteristics of the pendulum-like PZT layers. By doing such an exploration, the contactless nature of magnetic force can also be utilized in order to determine the characteristic outputs of the system. Thus, the lifetime of the PZT material is dramatically increased.

Excitation by magnetic flux has been explored for some decades in order to increase the efficiency of different harvester systems in terms of wide-band vibrations.^{8,9} A number of models and designs have been proposed in the literature with that in mind.⁸⁻¹⁰ For example, a harvester with four permanent magnets in a stable magnetic field was proposed by Cottone et al.⁸ Their system operates as an inverted pendulum, and the dynamics of stochastically nonlinear vibrations and corresponding energy outputs were examined. In another paper, Ferrari et al.¹ proved that the wide-band vibrations exerted by the permanent magnets can improve the output power up to 250%; indeed, the nonlinearity in their field assists in enhancing the harvested power. In addition, in one of our earlier studies,^{11,12} we have proven that, if a periodic magnetic field is used in place of a stable field, the responses of the PZT layer can entirely differ from the findings of Ferrari et al.¹ Strictly speaking, the harvested power dramatically decreases. These two results from different systems have motivated us to explore the behavior of the buckling PZT layer. The characteristics of the field can yield to different results in different systems. The reason for such different results is considered to be the bistable excitation of the system in Ref. 1. If the system has two equilibrium positions, it can yield to a better harvesting mechanism. Such a system can be constructed by either considering only the mechanical aspects of the system or introducing an external nonlinear force as in Ref. 13. Indeed, the bistability drives the system from one state to the other by resulting large amplitudes in position. The intermediate regimes of the bistable mode survive for appropriate parameter sets and yield to large amplitude oscillations. That transition from the monostable to the bistable state causes larger displacements, thereby the amount of the obtained energy increases dramatically as was also pointed out by Ferrari et al.¹ However, in the case of a nonautonomous magnetic field, as in our earlier papers,^{14,15} the complicated responses of the layer have been observed experimentally and theoretically. The dynamic responses such as periodic and chaotic states have been observed and even bistable modes have also been encountered for

certain parameter ranges. Thus, further work on the matter is required in order to clarify the results. Similar analyses have proved that the nonlinear systems can generate large-amplitude oscillations over a wider frequency range with respect to the linear case,^{16,17} and thus high amounts of power can be generated under proper conditions. The characteristic feature of an individual system needs to be examined both theoretically and experimentally in order to sketch out the overall dynamics and energy conversion mechanism. The conversion mechanism is essentially affected by electrical load, excitation frequency and the distance to the excitation source, and these have not yet been fully explored.

Energy harvesters can be electromagnetic or electrostatic, whereas energy densities of PZT systems become much higher around 35 mJ/cm³ compared to pure electromagnetic or electrostatic systems.^{11,18} In addition, PZT systems can harvest higher voltages up to 15 V compared to electromagnetic energy converting systems for a small layer.¹⁹ Therefore, PZT harvesters become much promising for various engineering applications. In addition to their high energy densities, the compact nature makes them suitable for many micro-electromechanical systems (MEMS).¹⁹

In the present paper, we report further effects of the periodic magnetic field excitation for a PZT layer in order to carry out an optimization study on the energy harvesting mechanism. Apart from the previous studies,^{5,12} the piezoelectric layer has been mounted on a propeller via a shaft and a varying higher magnetic force exerted on the tip of the layer due to higher magnetic flux density of the permanent magnet. In addition, a wide parametrical survey has been performed for magnetic force (i.e. coil voltage U_c) and rotation frequency ω . The dynamic responses of the layer have been identified for these parameters. The findings can be easily adapted to a harvester system, positioned close to a generator, relay or electric motor, which can exert a periodic magnetic ambient (see, for instance, Refs. 20–22). The present work also includes the description of the nonlinear magnetic force in the vicinity of the layer and describes the estimated power from a layer by using the system parameters. “[Experimental](#)” section gives an experimental overview for the proposed wind energy. A detailed analytical description of the harvester is presented in “[Theoretical Background](#)” section. The main findings from the simulations based on the analytical description and the experiments are discussed in the next section. Finally, the paper ends with concluding remarks.

EXPERIMENTAL

The Proposed New Wind Energy Harvester

The new wind harvester consists of four units as shown in Fig. 1. The first unit is a propeller rotated by the wind. The second unit is the shaft conveying the mechanical rotation to the magnet and the third

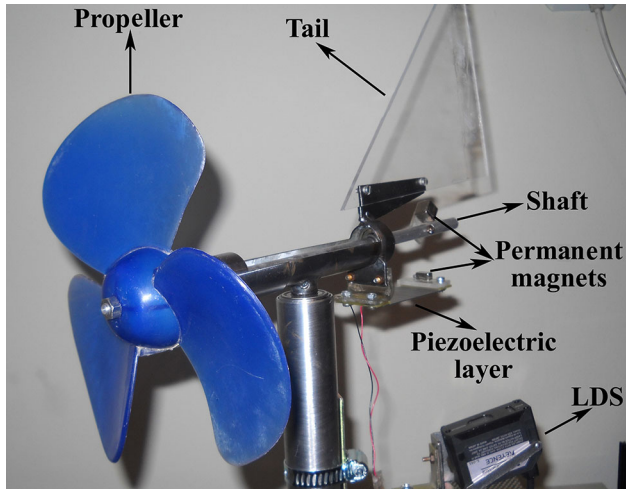


Fig. 1. The new piezoelectric wind harvester with increased magnetic force by magnets.

is the static piezoelectric unit generating the electrical energy. Finally, the last unit is the electronic part regulating the harvested electrical signal from the output terminals of the PZT. In a previous study,⁵ we proposed a design and implementation of a low-field harvester model, since the magnets used in this prototype were smaller, with 0.3 T magnetic flux density in its air gap. In the present work, the magnetic flux density has been increased to 0.45 T in the air gap between the shaft magnet and the layer one.

The harvester has a length of 30 cm from propeller to the end of the tail. The PZT layer has the dimensions of 70 mm × 32 mm × 1.5 mm and a weight of 10 g. The diameter of the propeller is 16 cm and it can move easily with the help of a small gear inside the body. The harvester body has been made by a stainless steel material with 1 mm thickness in a cylindrical shape and it has a diameter of 2 cm. The shaft is made from an aluminium rod with 5 mm thickness and is connected to the center of the propeller from the front and a cubic magnet has been located at the back. The piezoelectric layer is in contact with the bottom part of the harvester body and another magnet of 1 cm length and 4 mm thickness has been added to the opposite end of the layer. Note that that part is larger than the previous machine referred to in Ref. 5. Thus, we measured higher flux density as stated above. The air gap magnetic flux density has been measured by a Bell-5170 gaussmeter. The lowest distance between the two magnets is 2.5 mm when the machine operates.

The proposed harvester includes two permanent magnets, which are located opposite to each other while the shaft rotates. One PZT stands on the shaft and the other stands on the stable body. The magnets and their locations are shown in Fig. 1. A Plexiglas light tail directs the propeller to the wind

flow. When the wind comes onto the blades, the shaft can rotate freely about the shaft axis, which helps to rotate the magnet on the shaft. The magnet repels the tip of the PZT material, where the other magnet has been positioned. When the magnet comes closer to the magnet which is attached to the tip of the PZT layer, the layer is bent downwards without any mechanical contact, since the poles of the magnets are the same. Thus, the mechanical energy is converted to electricity. According to the preliminary tests, a magnetic flux density of 150 Gauss can occur between the two magnets when they become close to each other. Thus, this becomes sufficient to repel the tip of the layer by resulting oscillations.

Vibration Tests of the Piezoelectric Beam

The experimental setup for the test of the PZT layer of the proposed harvester is presented in Fig. 2. The setup consists of the following units: the ferromagnetic beam with a piezoelectric layer (PZT), the magnetic excitation unit, rectifier and storage circuit, signal generator, laser displacement sensor (LDS) and data acquisition and monitoring units.

The moving part of the system is arranged as a pendulum including a ferromagnetic cubic knob having the dimensions 10 mm × 10 mm × 10 mm (see inset of Fig. 2). The PZT layer is positioned at the top of the pendulum connecting the non-ferromagnetic beam to the clamp.

The vibration test equipment can be used for different parameters such as the distance between the magnet and the electromagnet, different piezoelectric materials and electrical loads, etc. The L-shaped stainless steel piezoelectric holder has a height of 21 cm. The horizontal length of the holder is 10 cm, which enables the vibration of the layer back and forth. The distances between the tip magnet and the core tip of the electromagnet have been adjusted from 3 cm to 2 mm by applying several winding currents. This system has been beneficial for examining the vibration of the piezoelectric material for different magnetic effects. In traditional shaker experiments, one can give a mechanical thrust to the layer, whereas the aim here is the determination of the vibration characteristics under the magnetic force. Note that Eq. 7 in the next section gives a complete definition for the mathematical statement of that magnetic force applied from that system.

An external saw-teeth-like magnetic force (f_m) is exerted to the pendulum through the electromagnet during the tests. An electromagnet is used to produce certain frequency oscillations on the beam and the output signal is observed experimentally.

The vibrations are mainly formed by the attractive force of the magnetic force and the elastic force of the PZT layer. There also exist damping effects, which can be measured during the

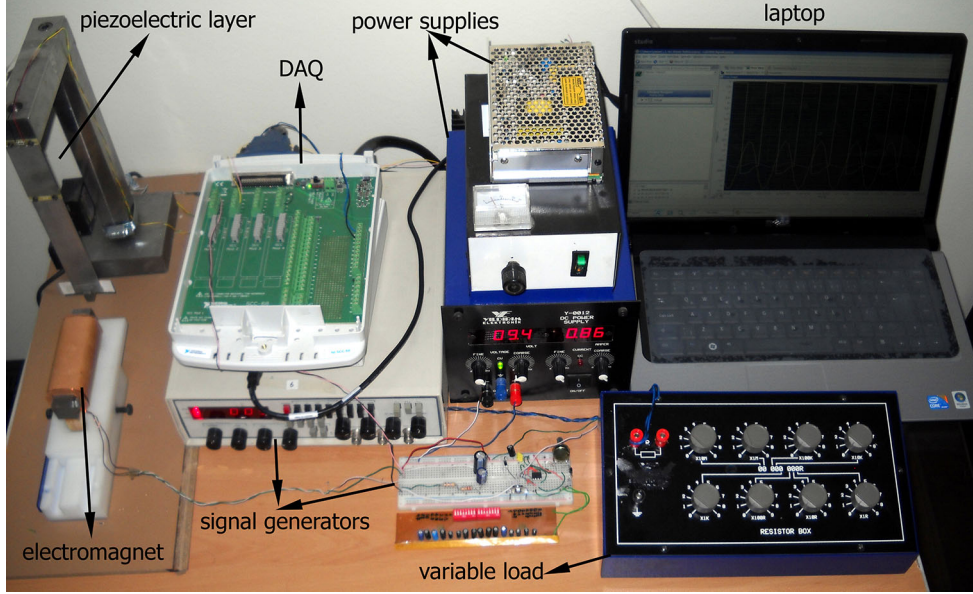


Fig. 2. The experimental test setup for the harvester PZT.

experiments. A laser displacement sensor has been located for the measurement of tip displacement. Both the magnetic excitation data (i.e. waveform) and the output signal of the PZT can be recorded synchronously. Since the main parameters are the amplitude and frequency of the excitation waveform, the dynamics of PZT can be explored for wide ranges from 0.5 Hz to 50 Hz. If much suitable excitation strength (i.e. $U_c = 4\text{--}10\text{ V}$) is adapted to the electromagnet, the damping effects can be basically ignored and the elastic forces can compete with the field excitation.

In the experiments, a PZT layer made by Piezo System has been used. It has the sizes of $70\text{ mm} \times 32\text{ mm} \times 1.5\text{ mm}$ and a weight of 0.01 kg. According to the manual, the capacitance and stiffness of the PZT layer are 232 nF and 188 N/m, respectively. The LDS has an IL-065-type head controller IL-1000 which was made by Keyence. The sensor head can measure the vibrations with the sampling rate of $t = 1\text{ ms}$. In the experiments, a rectifier, storage circuit, signal generating circuit for step pulsed signals and an NI USB-6250 data acquisition card have been used. The data acquisition card has 16 analog inputs and enables the making of multiple recordings of quantities such as the displacement of the layer tip and input/output voltages.

The electromagnet has 1050 turns of 0.70-mm-diameter copper wires. The dimension of its core is $120\text{ mm} \times 20\text{ mm} \times 20\text{ mm}$ and it has a relative permeability of $\mu_r = 10,000$. The step-pulsed voltage is characterized by its amplitude U and frequency f . All experimental outputs can be collected via the LabVIEW software. To examine the PZT behavior at different distances between the tip and the

electromagnet, the distance d can be adjusted with an appropriate sliding mechanism. The terminals of the PZT have been attached to an electrical load R_L .

THEORETICAL BACKGROUND

The theoretical statement of the proposed harvester can be written as follows:

$$\frac{d\theta}{dt} = \omega, \quad (1)$$

$$m \frac{d^2 r}{dt^2} = ku(t) + \alpha V(t) + f_m \delta(\theta - \theta_0), \quad (2)$$

$$I(t) = \alpha \frac{du(t)}{dt} - C \frac{dV(t)}{dt}, \quad (3)$$

where, θ , ω , δ , m , r , u , α , V , f_m , θ_0 , C , I and k indicate the angular position of the magnet, the propeller speed, Kronecker delta which gives 1 for $\theta = \theta_0$ else 0, the mass of the layer, the radial position to the center of the shaft, the mass displacement of the layer, the force factor of the layer, the voltage between the layer terminals, the magnetic force of the magnet, the angular position of the layer, the layer capacitance, the harvested current and the stiffness constant of the layer, respectively. For a more detailed expression, we refer to our previous studies.^{5,6,11}

In order to analyze the PZT layer which is denoted in Eqs. 2 and 3, the layer can be modeled as in Fig. 3. In the present model, an external magnetic field obtained by an electromagnet is considered to affect a ferromagnet knob attached to a piezoelectric layer.

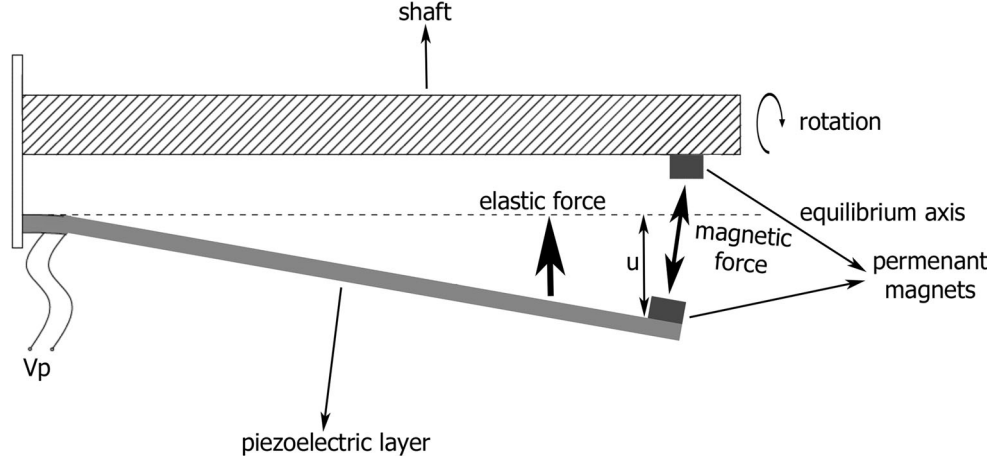


Fig. 3. The modeling of a PZT layer in the vicinity of an electromagnet.

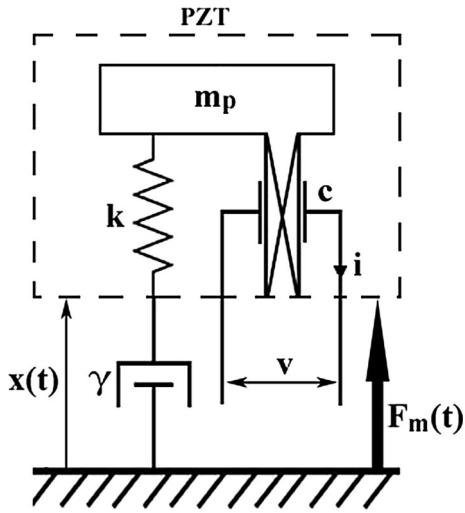


Fig. 4. The energy harvesting procedure of the PZT layer under a varying magnetic field due to the rotation.

The electromagnet generates a saw-teeth-like magnetic force near the tip. The dynamics of the pendulum-like beam consists of a certain elastic force, gravitational force and magnetic force as in Ref. ¹⁵. In the present model, the elastic force is much higher than the gravitational force, thus the gravitation can be neglected. ^{14,15,21} The algebraic modeling in Eqs. 1–3 can be clarified by considering Fig. 4.

In that model, a mass-spring, a damper and a capacitor are considered. Here, F_m , which is produced by the magnet with certain periods is modeled by the excitation frequency of the oscillating field. Here, the rigid mass m_p and the stiffness constant k determine the mechanical structure under a damper γ giving the mechanical losses. If a mass displacement u occurs in the PZT layer, an electrical current I and a voltage V are produced.

The relationship between the mechanical and electrical units is given by the following equation system:

$$\begin{aligned} F_{\text{total}}(t) &= ku(t) + \alpha V(t) + F_m(t), \\ I(t) &= \alpha \frac{du(t)}{dt} - C \frac{dV(t)}{dt}. \end{aligned} \quad (4)$$

The equations include the backward piezoelectric coupling. Here, C is the clamped capacitance and α is the force factor. In addition, V denotes the harvested voltage of the PZT and I gives the current when an electric load R_L is attached to the system. Then, the total equation of motion for the displacement of mass, $u'(t)$, as a result of the pendulum tip displacement $x'(t)$ is given as,

$$\begin{aligned} (m + m_p) \frac{d^2 x'(t)}{dt'^2} &= -\gamma \frac{du'(t)}{dt'} - m_p \frac{d^2 u'(t)}{dt'^2} \\ &\quad - ku'(t) - \alpha V(t) - F_m(t). \end{aligned} \quad (5)$$

Considering the electrical part and x' , which has been adjusted to 3 times the displacement u' of the PZT layer, one defines $u' = 0.33x'$. Then, the dynamic equation can be stated as,

$$\begin{aligned} \frac{d^2 u'(t)}{dt'^2} &= -\frac{\gamma}{3m + 4m_p} \frac{du'(t)}{dt'} - \frac{ku'(t)}{3m + 4m_p} \\ &\quad - \frac{\alpha V(t)}{3m + 4m_p} - \frac{F_m(t)}{3m + 4m_p}, \\ \frac{dV'(t)}{dt'} &= \frac{\alpha}{C} \frac{du'(t)}{dt'} - \frac{I(t)}{C}. \end{aligned} \quad (6)$$

The resulting equations describe the electromechanical model of the harvester problem. The magnetic force with changing frequency can be described as in Ref. 11. The magnetic force has two main quantities: the distance d from the electromagnet to the PZT tip and the winding current as described below:

$$F_m(x) = \left\{ \begin{array}{l} \left\{ (1 - 0.7056/d) + 0.0623(1 - 3u) + 28026d(1 - 3u)^2 - 10^6d^2(1 - 3u)^3 \right\} \\ \left\{ \alpha \left(\frac{U_c}{R_c} (1 - e^{-R_c t/L}) \right)^2 - \beta \frac{U_c}{R_c} (1 - e^{-R_c t/L}) \right\} \quad 0 < t \leq \frac{T}{2} \\ \left\{ (1 - 0.7056/d) + 0.0623(1 - 3u) + 28026d(1 - 3u)^2 - 10^6d^2(1 - 3u)^3 \right\} \\ \left\{ \alpha \left(\frac{U_c}{R_c} e^{-R_c t/L} \right)^2 - \beta \frac{U_c}{R_c} e^{-R_c t/L} \right\} \quad \frac{T}{2} < t \leq T \end{array} \right\} \quad (7)$$

Here, U_c , R_c , and L represent voltage, resistance and inductance of the electromagnet, respectively. For clarity, the electromagnet force constants are defined from the simulation as $\alpha = 8 \times 10^{-8}$ and $\beta = 10^{-9}$.

The dimensionless statement of Eq. 6 is found when $t' = \tau t$, $y' = yd/\tau$, $u' = ud$ and $V' = V_0V$ are introduced for the time, velocity, position and voltage scaling, respectively. Note that τ determines the natural period of the layer. Then, one arrives at,

$$\begin{aligned} \frac{du}{dt} &= y, \\ \frac{dy}{dt} &= -\frac{\gamma\tau}{3m + 4m_p}y - \frac{k\tau^2}{3m + 4m_p}u \\ &\quad - \frac{(m + m_p)\tau^2 F_m(t)}{(3m + 4m_p)d} - V \frac{\alpha\tau^2 V_0}{(3m + 4m_p)d}, \\ \frac{dV}{dt} &= \frac{\alpha d}{CV_0} \frac{du}{dt} - \frac{\tau V}{V_0 CR_L}. \end{aligned} \quad (8)$$

These first-order equations can then be used in the simulations and time integration via using the Runge–Kutta method. Here, d transfers the coordinate system into the equilibrium point of the pendulum, since the amplitude of the piezoelectric layer tip is represented by u . The preliminary experimental studies have proven that the natural frequency of the PZT layer is $f_0 = 4.76$ Hz, the damping constant $\gamma = 1.48$, and the ratio of elastic constant to mass $k/m = 894$. By introducing these parameters and Eq. 8 to MatLab, the solutions have been obtained after time integrations via the fourth-order Runge–Kutta method.

$\langle P \rangle$

$$= \frac{u^2 R_L \alpha^2 \omega_c^2 \{ (m + m_p) \omega_c^2 - F_0 \langle I_c^2 \rangle + F_1 \langle I_c \rangle \}^2}{k^2 (1 + C^2 R_L^2 \omega_c^2) + 2k \omega_c^2 (m_p + \alpha^2 C R_L^2 + C^2 m_p R_L^2 \omega_c^2) + \omega_c^2 \{ 2\alpha^2 \gamma R_L + \alpha^4 R_L^2 + 2\alpha^2 C m_p R_L^2 \omega_c^2 + \gamma^2 (1 + C^2 R_L^2 \omega_c^2) + m_p^2 \omega_c^2 (1 + C^2 R_L^2 \omega_c^2) \}} \quad (12)$$

In order to discover the averaged harvested power, Eq. 8 is initially recalled in the frequency domain. The voltage equation in Eq. 8 can be solved as,

$$V = \frac{jR_L \alpha \omega_c u}{1 + jCR_L \omega_c}, \quad (9)$$

in the frequency domain and, by considering the second equation in Eq. 8, we arrive at,

$$V = \frac{u R_L \alpha j \omega_c \{ (m + m_p) \omega_c^2 - F_0 \langle I_c^2 \rangle + F_1 \langle I_c \rangle \}}{(-j\gamma \omega_c - m_p \omega_c^2 - k)(1 + R_L C j \omega_c) - \alpha^2 R_L j \omega_c} + h.o.t., \quad (10)$$

after some arithmetic manipulation for the harvested voltage. The harvester is driven by the field frequency ω_c , therefore the solution should include ω_c . The linear terms of the piezoelectric displacement function u is included in addition to the field frequency. Note that $\langle I_c \rangle$ and $\langle I_c^2 \rangle$ indicate the time-averaged values of the electromagnet currents defined in Eq. 7 including α and β parameters. The averaged values are as follows:

$$\begin{aligned} \langle I_c \rangle &= \frac{U_c}{2R_c} + \frac{U_c L \omega_c}{2\pi R_c^2} \left(2e^{-\frac{R_c \pi}{L\omega_c}} - 1 - e^{-\frac{R_c 2\pi}{L\omega_c}} \right), \\ \langle I_c^2 \rangle &= \frac{U_c^2}{2R_c^2} + \frac{U_c^2 L \omega_c}{4\pi R_c^3} \left(1 - e^{-\frac{R_c 4\pi}{L\omega_c}} \right) + \frac{L \omega_c}{\pi R_c} \left(e^{-\frac{R_c \pi}{L\omega_c}} - 1 \right), \end{aligned} \quad (11)$$

during one period with a time integration. Above, the electrical parameters belong to the electromagnet when voltage U_c with an excitation frequency of $\omega_c = 2\pi f$ is applied. Thus, power is calculated as follows:

While using the linear part of Eq. 10 as function of u and its complex conjugate divided by the resistive load R_L (i.e. $\langle P \rangle = \langle VV^* \rangle / R_L$), Eq. 12 gives a complete relationship between the output power and

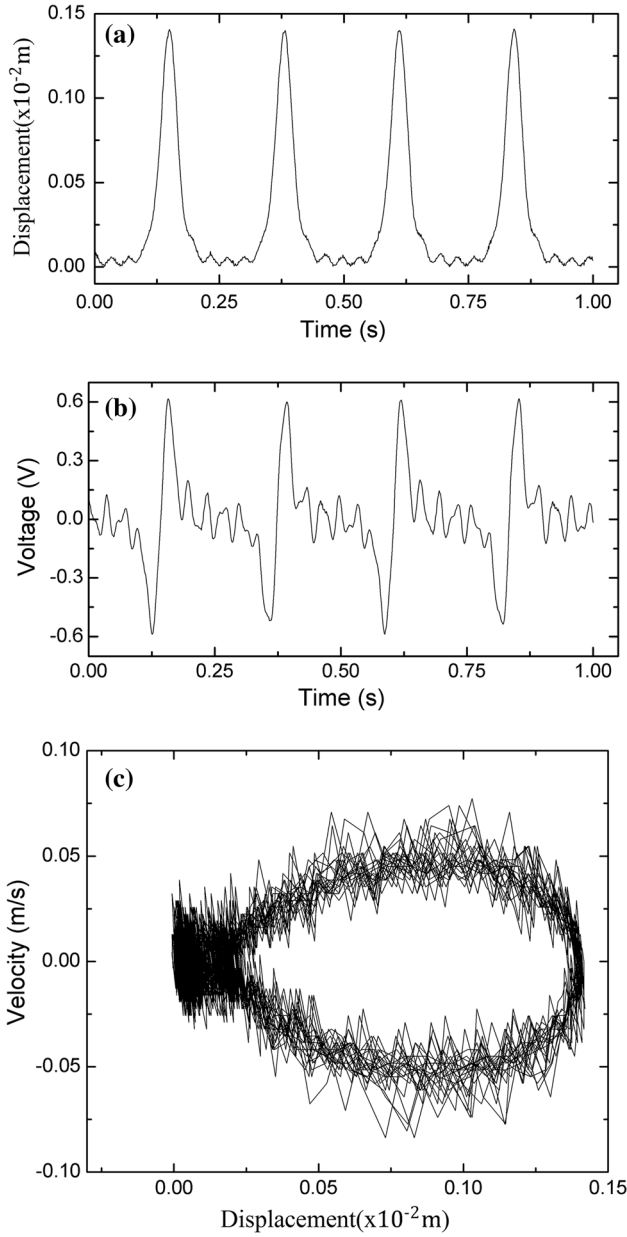


Fig. 5. (a) Displacement of the harvester layer tip from the equilibrium point. (b) Voltage waveform from piezoelectric terminals. (c) The attractor for the wind speed of 3.5 m/s.

both the electrical and mechanical parameters of the system.

RESULTS AND DISCUSSION

Experimental Discussion

In Fig. 5a, b, and c, displacement, velocity and voltage data are shown. These data have been received from the harvester shown in Fig. 1. The wind speed is 3.5 m/s for the wind tunnel. The displacement waveform has certain peaks at 0.15 cm; however, there exist ripples around the equilibrium point (Fig. 5a). The displacement occurs at the positive part where the magnet shaft

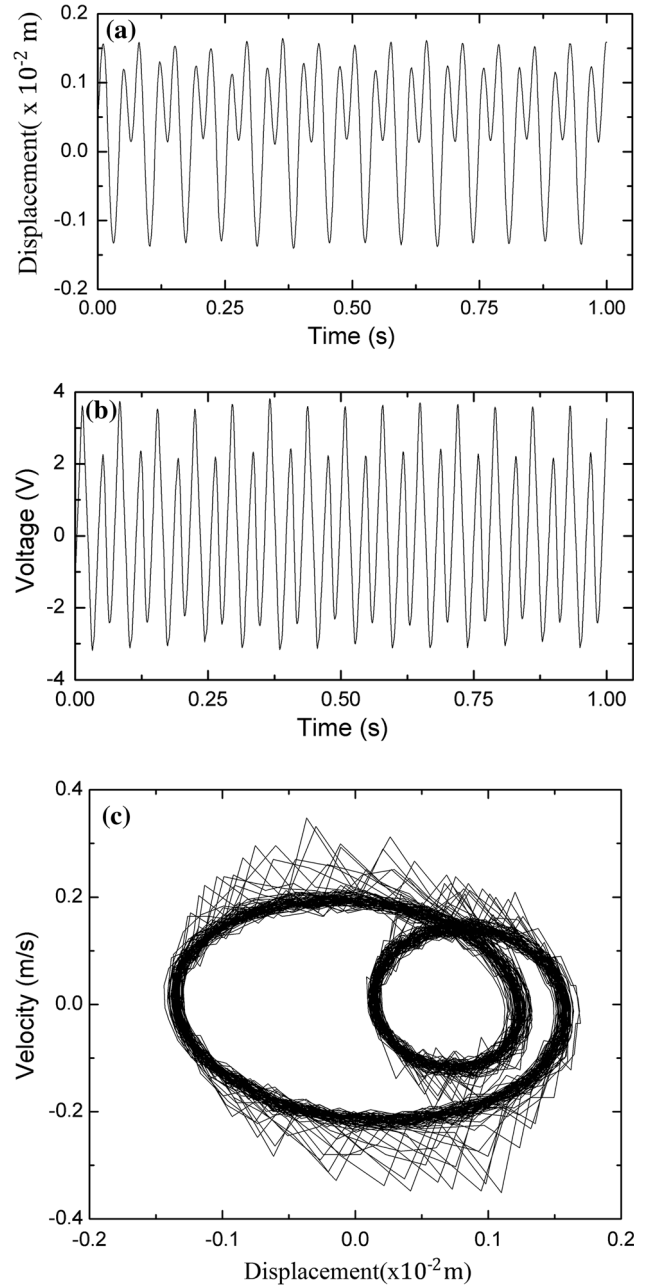


Fig. 6. (a) Displacement of the harvester layer tip from the equilibrium point. (b) Voltage waveform from piezoelectric terminals. (c) The attractor for the wind speed of 8 m/s.

always repels the tip of the piezoelectric and the layer cannot find sufficient time to continue its motion in the opposite displacement side. Such behavior is common for some wind speeds and has been encountered in many studies.^{1,11,12} Similarly, the voltage waveform also has certain peaks, where the displacement becomes maximum as in Fig. 5b. Peak to peak, 1.2 V can be generated at that speed, whereas the waveform includes harmonics, which affect the output power of the system. The voltage has been measured directly from the piezoelectric terminals without any electrical load in order to see

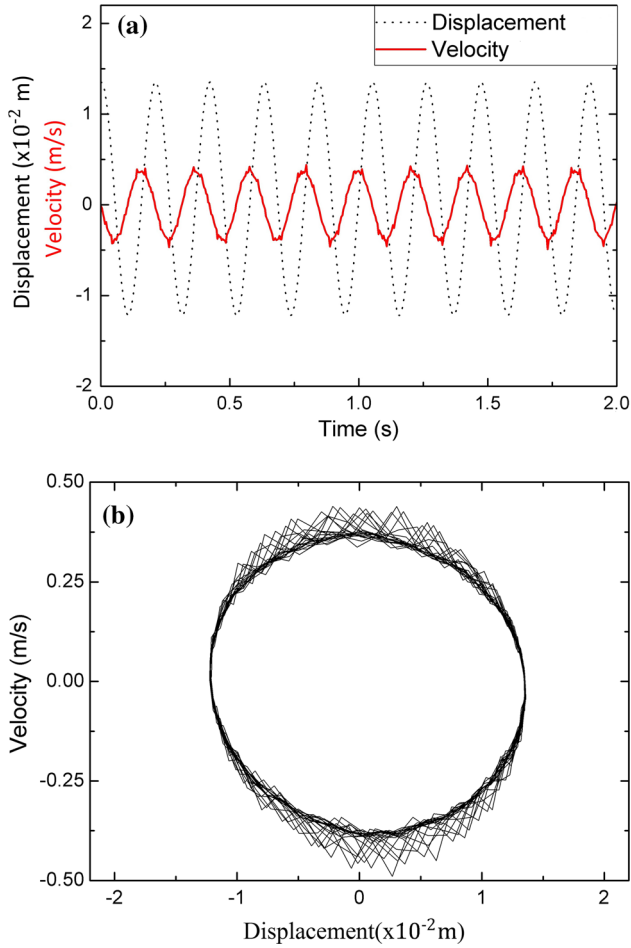


Fig. 7. (a) The vibrational test of the layer tip at $\omega_c = \omega_0 = 4.76$ Hz and $U_c = 6$ V as in Ref. 12. (b) The attractor from the data in (a).

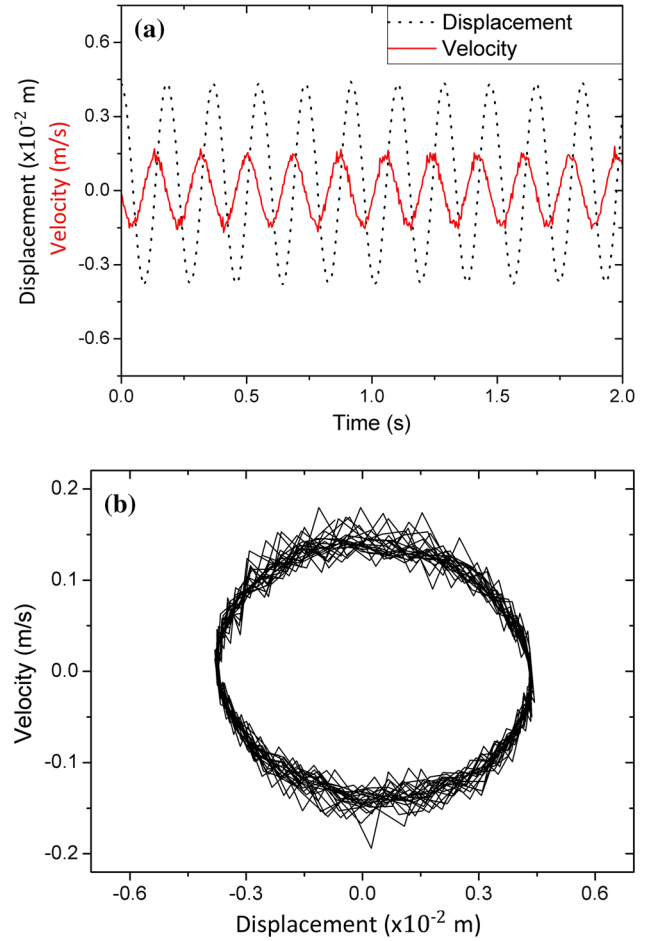


Fig. 8. (a) The vibrational test of the layer tip at $\omega_c = 1.14\omega_0 = 5.43$ Hz and $U_c = 6$ V. (b) The attractor from the data in (a).

the pure waveform. In order to show the dynamic regime, the attractor is shown in Fig. 5c.

Another measurement is depicted in Fig. 6a, b, and c for higher wind speed (i.e. 8 m/s). It is obvious that displacement of the layer tip changes between negative and positive values due to the high speed (Fig. 6a). In addition, the waveform of displacement and corresponding voltage also change. The peak to peak value reaches to 6.5 V with a distorted form in a long time period (Fig. 6b). The voltage has been obtained directly from the piezoelectric terminals without the electrical load. By considering Figs. 5 and 6, we aim to show the characteristic outputs of the piezoelectric. This distortion can be seen clearly from the attractor in Fig. 6c. The ripples of that double scroll attractor are due to magnetic force as also encountered at lower speeds. The similar double scroll attractors have also been found from the theory and are presented in the next section.

The attractors above prove that the proposed model is sufficient for the determination of the harvester dynamics and power relationships. In

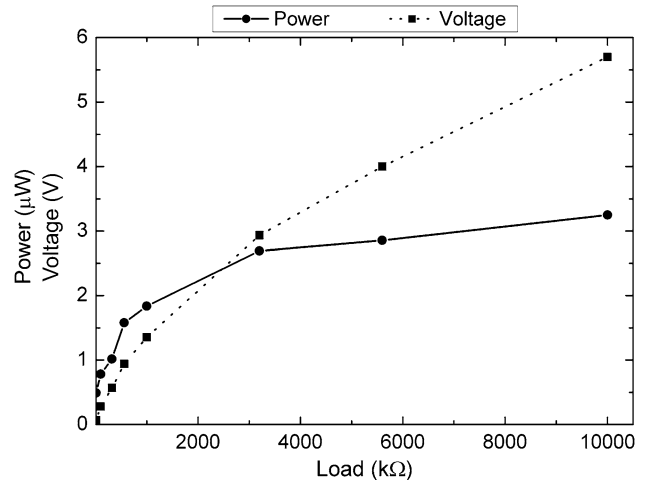


Fig. 9. Rectified output voltage and output power for the wind speed 3.5 m/s.

order to test the vibrations at various frequencies, some controlled experiments have been carried out with the setup in Fig. 2. The results of displacement

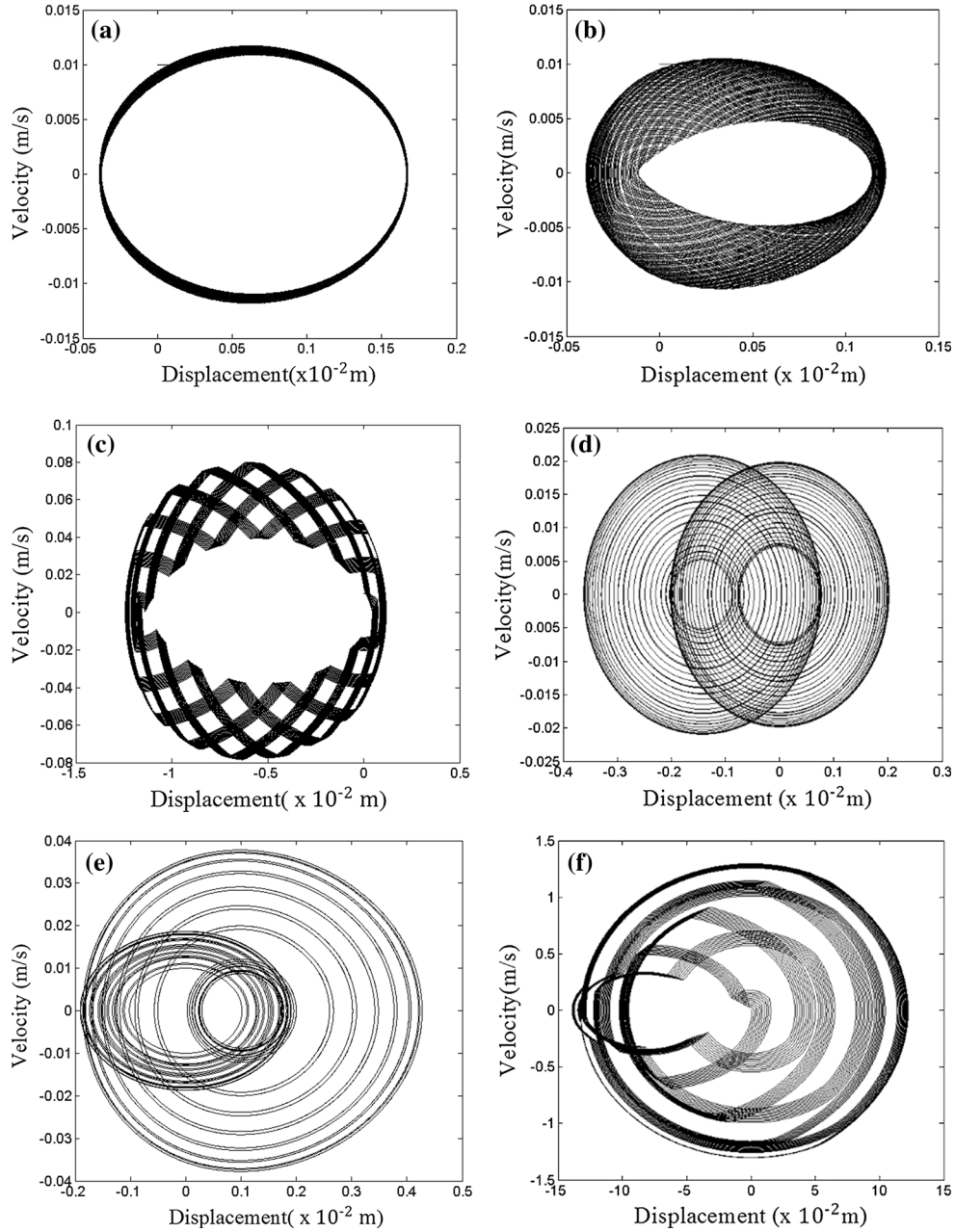


Fig. 10. The attractors (i.e. phase space representations) from displacement versus velocity data from simulations (a) from the periodic regular region in Fig. 11 at $(U_c, \omega_c) = (4 \text{ V}, \omega_0 \text{ Hz})$, (b) from the chaotic region in Fig. 11 at $(U_c, \omega_c) = (4.27 \text{ V}, 6\omega_0 \text{ Hz})$, (c) from the saw-teeth chaotic region in Fig. 11 at $(U_c, \omega_c) = (7.21 \text{ V}, 4\omega_0 \text{ Hz})$, (d) from the double scroll chaotic region in Fig. 11 at $(U_c, \omega_c) = (5.61 \text{ V}, 35\omega_0 \text{ Hz})$, (e) from the triple scroll chaotic region in Fig. 11 at $(U_c, \omega_c) = (3.74 \text{ V}, 50\omega_0 \text{ Hz})$, and (f) from the multiple scroll chaotic region at $(U_c, \omega_c) = (9.35 \text{ V}, 10\omega_0 \text{ Hz})$.

and velocity are given in Fig. 7a and b at a natural frequency (i.e. $\omega_0 = 4.76 \text{ Hz}$) and $U_c = 6 \text{ V}$.

The experimental displacement and velocity time evolution in Fig. 7a have sinusoidal waveforms in accordance with our earlier studies.¹² As an indicator of magnetic force, there exist high-frequency ripples around the minimal and maximal values of velocity. This kind of effect will also be shown in the theory in the next section. In order to see the attractor in the phase space, Fig. 7b is depicted. Here, the ripples are much observable than at the

upper and lower regions, and they govern the dynamics and enhance the irregularities of the waveforms such as velocity and voltage.

Another displacement and velocity test result for slightly higher excitation frequency is given in Fig. 8. While the displacement is still in sinusoidal waveform, the ripples in the velocity data increase further for all waveforms (Fig. 8a). This effect can be seen clearly from the attractor in Fig. 8b. The chaos governs the phase space and the peak to peak values decrease compared to the case in Fig. 7a and

b. Thus, that also causes a decrease in the harvested voltage.

The harvested voltage and power, which have been received from the terminals of the rectifier, are shown in Fig. 9. Note that the generated voltage and power strictly depend on the impedance balance between the electrical load at the output and the internal impedance. According to the technical feature of the piezoelectric layer, the maximal power can be obtained for $R_L = 10 \text{ M}\Omega$. Beyond that value, the power decreased as also proven in Ref. 11. It has been proven that the proposed piezoelectric harvester can be used for micro-watt consuming systems such as sensor nodes, alarm devices, etc.

Theoretical Discussion

The vibration analysis of the PZT layer under the saw-teeth-like force has been carried out mainly for two parameters: the excitation frequency (ω_c) of the field and the magnetic force strength (i.e. the maximal voltage of electromagnet U_c). These parameters have been explored in a wide region. Strictly speaking, the frequency range changes from $\omega_c = 0.1$ to 240 Hz and the maximal voltage range changes from $U_c = 1.5$ to 14 V. The buckling of the layer produces many different dynamical behaviors from periodic to chaotic. There also exist various types of attractors for different parameters. Figure 10 presents sample attractors from these simulations.

While Fig. 10a represents the periodic buckling of the layer resulting from a simple elliptical trajectory at $(U_c, \omega_c) = (4 \text{ V}, 119 \text{ Hz})$, Fig. 10b shows the trajectories at higher frequencies (i.e. 28.6 Hz) and excitation voltages (i.e. 4.27 V). When the magnetic force is increased further by increasing the voltage (i.e. 7.21 V), the trajectories in Fig. 10c are obtained. The main difference is the increase in the displacement and velocity at that parameter. Note also that the saw-teeth appearance at the lateral regions of the ellipse trajectory occurs due to the lower frequency relative to Fig. 10b. The phase plane becomes more different when the frequency is

Fig. 12. The corresponding voltages for (a) from the periodic regular region in Fig. 11 at $(U_c, \omega_c) = (4 \text{ V}, \omega_0 \text{ Hz})$, (b) from the chaotic region in Fig. 11 at $(U_c, \omega_c) = (4.27 \text{ V}, 6\omega_0 \text{ Hz})$, (c) from the saw-teeth chaotic region in Fig. 11 at $(U_c, \omega_c) = (7.21 \text{ V}, 4\omega_0 \text{ Hz})$, (d) from the double scroll chaotic region in Fig. 11 at $(U_c, \omega_c) = (5.61 \text{ V}, 35\omega_0 \text{ Hz})$, (e) from the triple scroll chaotic region in Fig. 11 at $(U_c, \omega_c) = (3.74 \text{ V}, 50\omega_0 \text{ Hz})$, and (f) from the multiple scroll chaotic region at $(U_c, \omega_c) = (9.35 \text{ V}, 10\omega_0 \text{ Hz})$.

increased up to 166.6 Hz. Although the excitation voltage is adjusted lower than in Fig. 10c, the system generates two main attracting centers on the phase plane. The displacement of the tip also increases and from time to time it skips to the other center. Although the velocity becomes lower relative to the case in Fig. 10c, we expect that the power production can increase due to that larger displacement. When the excitation voltage is decreased further and the frequency is increased, the attractor in Fig. 10e is obtained. While the velocity data double compared to Fig. 10d, the displacement does not change very much. However, when the displacement becomes larger than a certain value, the other attracting point attracts the tip and the tip continues to oscillate around the electromagnet with lower displacement and velocity. If the displacement increases further, another limit of the displacement is exceeded and the system comes back to the previous attracting point. If the excitation voltage is increased much higher and the frequency is decreased to 47.6 Hz, both the displacement and velocity are dramatically increased. While that scenario can be possible in simulations, one should be careful in the real experiments in the sense that such a high voltage (i.e. magnetic force) may break the PZT layer. In that case, although theoretically much energy is harvested at this parameter set, it may be impossible to reach that scenario in the real world. Thus, careful tests should be carried out in order to optimize the harvester force. Indeed, the phase space trajectories resemble the case in Fig. 10e, although the values become higher.

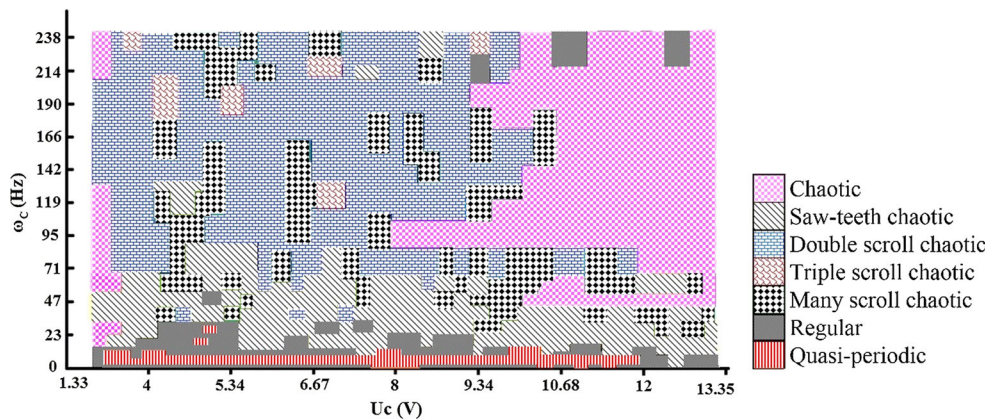
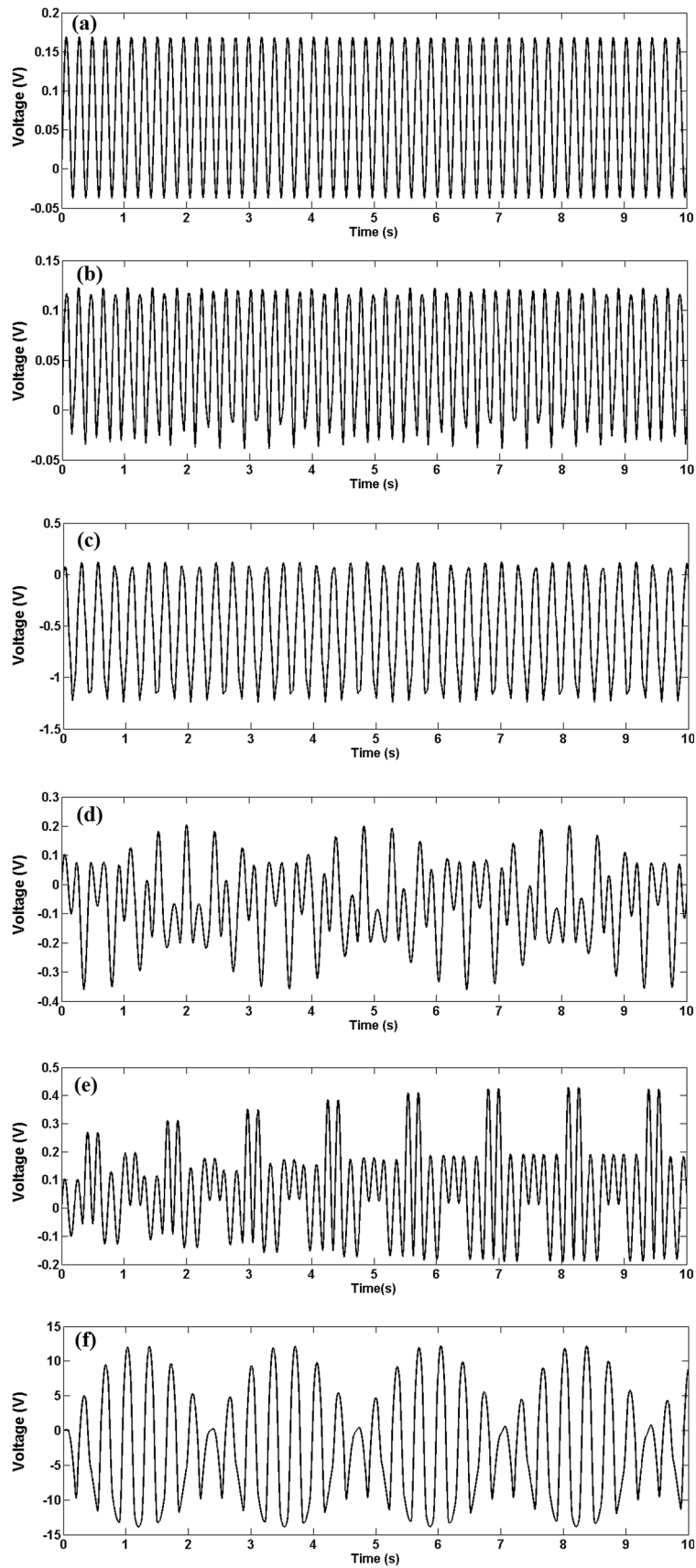
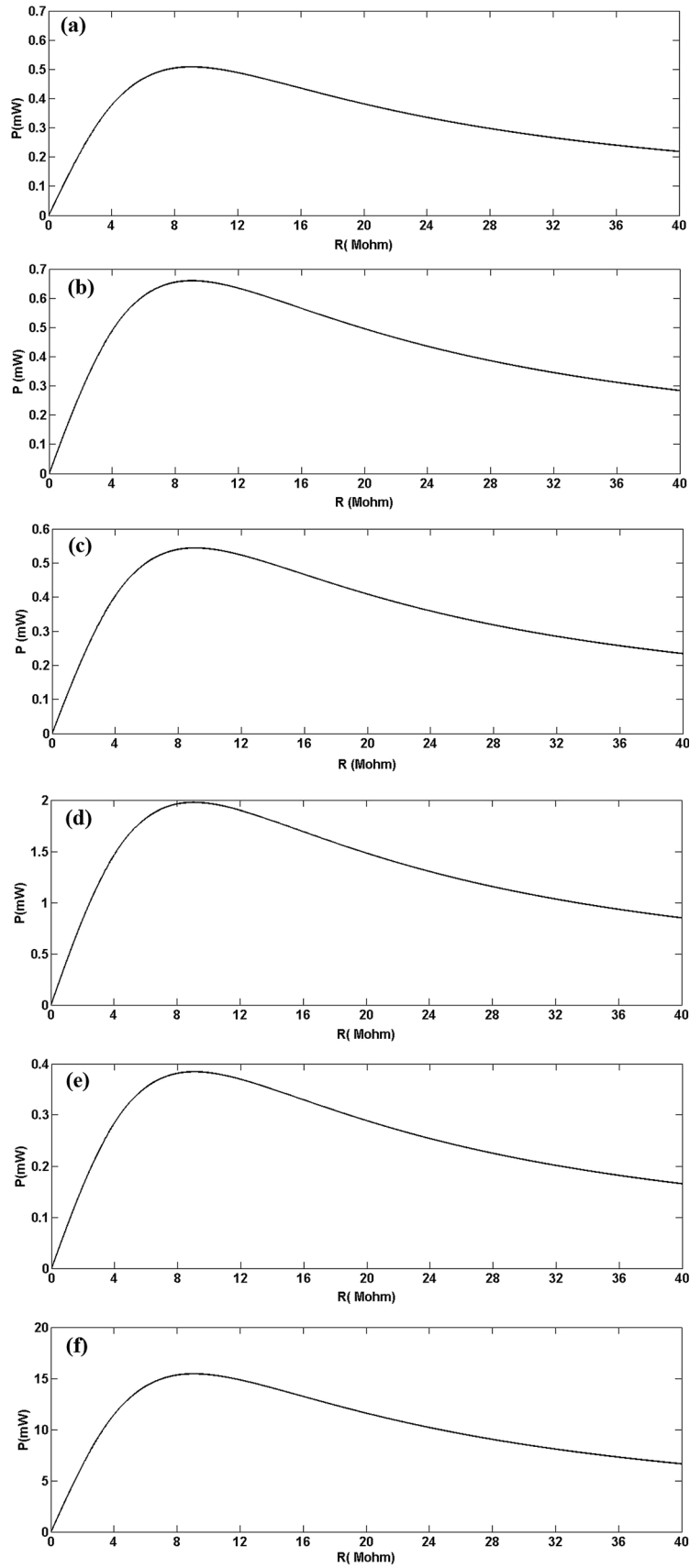


Fig. 11. The dynamics depending on the excitation voltage (i.e. the indicator of magnetic force) and excitation frequency.

Experimental and Theoretical Explorations on the Buckling Piezoelectric Layer Under Magnetic Excitation





◀Fig. 13. The harvested power for (a) from the periodic regular region in Fig. 11 at $(U_c, \omega_c) = (4 \text{ V}, \omega_0 \text{ Hz})$, (b) from the chaotic region in Fig. 11 at $(U_c, \omega_c) = (4.27 \text{ V}, 6\omega_0 \text{ Hz})$, (c) from the saw-teeth chaotic region in Fig. 11 at $(U_c, \omega_c) = (7.21 \text{ V}, 4\omega_0 \text{ Hz})$, (d) from the double scroll chaotic region in Fig. 11 at $(U_c, \omega_c) = (5.61 \text{ V}, 35\omega_0 \text{ Hz})$, (e) from the triple scroll chaotic region in Fig. 11 at $(U_c, \omega_c) = (3.74 \text{ V}, 50\omega_0 \text{ Hz})$, and (f) from the multiple scroll chaotic region at $(U_c, \omega_c) = (9.35 \text{ V}, 10\omega_0 \text{ Hz})$.

In Fig. 11, an overall summary of the dynamical behavior is given. This 2D diagram is vital, since it can estimate the dynamical characteristics of the system. In the diagram, all colors correspond to different dynamical phase space trajectories from periodic ones to various chaotic ones. According to that figure, the dynamics are governed in mainly two regions (i.e. blue and red): double scroll chaotic (as in Fig. 10d) and exponentially increasing circular chaotic regimes. Note that the exponentially increasing circular regime has much larger diverging trajectories, hence it is separated from the saw-teeth chaotic regime. This occurs when the magnetic force exceeds a limit value (i.e. excitation voltage $U_c = 9.35 \text{ V}$) as expected, because the increasing magnetic force attracts the dynamics strongly as an energy source. Thus, it yields to give energy to the system and causes a rapid increase in the distance of the trajectories. Indeed, the saw-teeth chaotic regime governs the dynamics for lower frequencies, namely lower than $\omega_c = 90 \text{ Hz}$. However, it survives for all magnetic forces (i.e. excitation voltages U_c) from 2.67 V to 13.35 V.

The non-chaotic periodic regime also survives for all excitation strengths, whereas it appears only for lower frequencies (i.e. $\omega_c = 24 \text{ Hz}$). Among the above-mentioned regions, there exist some certain islands for triple scroll chaotic and many scroll chaotic regimes.

In Fig. 12a, b, c, d, e, and f, the corresponding harvested voltages are given for all the attractors in Fig. 10. It is obvious that the periodic attractor gives a periodic voltage output on the resistive load as in Fig. 12a. The chaotic attractor in Fig. 10b gives a random voltage output as in Fig. 12b. Note also that the peak values become slightly lower than the periodic case. The harvested voltage of Fig. 10c has a weak undulation on the main frequency (see Fig. 12c). The reason for the undulation is nothing more than the low-frequency components which are apparent in Fig. 10c as the ripples. However, these ripples always have different values and lead to a weak chaotic output. The two-well attractor in Fig. 10d creates a similar characteristic voltage output as in Fig. 12d. The voltage always changes randomly and the scrolls can sometimes be seen at the upper and sometimes the lower part of the waveform.

Figure 12e gives a very chaotic appearance by changing the amplitudes. The maximal amplitude can have values between $V = 0.1 \text{ V}$ and 0.45 V . This characteristic property can also be seen in the phase

plane shown in Fig. 10e by defining the multiple scrolls. Note that, considering the maximal values of the waveforms, there is not much difference between the waveforms of the double scroll and the triple scroll chaos. The same property is also seen in the phase space trajectories. The last waveform in Fig. 12f has a relatively higher amplitude, which yields to a high power output. The waveform has several scrolls; however, only a short time is sketched in Fig. 12f for clarity.

The output powers for all types of dynamic regimes (from the simulations in Fig. 10) are shown in Fig. 13a, b, c, d, e, and f). The maximal power values changes from $380 \mu\text{W}$ to 16 mW in simulations depending on the dynamical regime. While the regular regime can harvest power up to $P = 520 \mu\text{W}$ as in Fig. 13a, the power can increase for higher values in the chaotic regimes. Such a situation, which proves the increase of power in nonlinear regimes, was also observed by Cottone et al.⁸ They reported in their study that the two-well chaotic structure, which corresponds to our double scroll regime, can induce larger distances from one attracting point to the other. Thus, that can result in an increase in output power. Our simulation results also support their findings in the sense that the power of the double scroll regime in Fig. 10d yields nearly 2 mW , which is much higher than the regular case in Fig. 10a. Another interesting observation from the simulations is that the saw-teeth chaotic regime also has higher harvested power with 6 mW . In one of our earlier studies,¹¹ we have proven that the saw-teeth structure in velocity data occurs due to the periodic magnetic excitation and that this regime is observed for lower excitation frequencies.

Although the frequency is low, small oscillations in displacement and velocity may produce larger power ranges. In addition, it can also be stated that the displacement in Fig. 10c is large compared to other regimes except for the case in Fig. 10f. Thus, this reason mainly causes the increase in power compared to the other cases. However, we cannot say that the ripples like saw-teeth do not influence the power extraction. In the cases of Fig. 10d and e, the displacements are nearly the same. However, the regime in Fig. 10e is nearly two times faster than the other one. However, the regime in Fig. 10d generates more power compared to the other case. That can be explained in such a way that the two scroll regime frequently transitions from one attracting point to the other. Thus, this transition on the phase plane causes an increase as in Ref. 8. In the triple scroll regime, there also exist several transitions; however, the trajectories stay for longer periods in each regime and that does not contribute to the power. The last regime, given in Fig. 10f, has the highest power result, since both the displacement and velocity are high compared to the earlier cases. However, that cannot be available in real experiments, since such a high excitation amplitude

can break down the PZT layer. However, it is also interesting to know that 16 mW of power can be obtained from the simulations for that system.

CONCLUSIONS

Both experimental and theoretical studies on the buckling characteristics of a wind energy harvester have been carried out. According to the findings, the layer tip exhibits a rich dynamics depending on the magnetic field strength and magnetic field excitation frequency. It has been proven that the periodic responses take place for the frequencies near the natural frequency of the layer. There also exist quasi-periodic responses for lower frequencies. The field strength and frequency directly affect the buckling and the harvested energy very greatly depends on these parameters. Indeed, double and multiple scroll dynamics appear for a large parameter set and they can produce better energy. This proves that the nonlinearities can assist in increasing the power for some parameter sets; however, it may also decrease the harvested energy for some parameters. The suggested model agrees well with the experiments and that model can predict the harvested power, displacement, velocity, voltage and current with a good accuracy. Thereby, the model can be utilized to improve the system for better power harvesting and the experimentalists can use the model to adjust the parameters for periodic excited harvesters. This detailed exploration also proves that one needs to design and implement a good rectifying system in order to solve the harmonic waveforms and store the energy. By considering the dependence on the electrical load, an efficient maximum power point tracking mechanism is also required. Further studies should be carried out to make use of the maximal power gain from the system.

ACKNOWLEDGEMENT

The authors are grateful to the European Union Ministry of Turkey, National Agency of Turkey, for the support of this project under the Project

Code: 2015-1-TR01-KA203-021342 entitled *Innovative European Studies on Renewable Energy Systems*.

REFERENCES

1. M. Ferrari, V. Ferrari, M. Guizzettia, B. Andò, S. Baglio, and C. Trigona, *Sens. Actuators A* 162, 425 (2010).
2. K.A. Cook-Chennault, N. Thambi, and A.M. Sastry, *Smart Mater. Struct.* 17, 1 (2008).
3. Y. Song, C.H. Yang, S.K. Hong, S.J. Hwang, J.H. Kim, J.Y. Choi, S.K. Ryu, and T.H. Sung, *Int. J. Hydrog. Energy* 41, 12563 (2016).
4. M.A. Karami, J.R. Farmer, and D.J. Inman, *Renew. Energy* 50, 977 (2013).
5. Y. Uzun, S. Demirbas, and E. Kurt, *Elektron. Elektrotech.* 20, 35 (2014).
6. Y. Uzun and E. Kurt, in *Proceedings of 11 International Conference on Applications of Electrical Engineering* (2012).
7. L. Mateu and F. Moll, in *Proceedings of the SPIE Microtechnologies for the New Millenium*, vol. 359 (2005).
8. F. Cottone, H. Vocca, and L. Gammaitoni, *Phys. Rev. Lett.* 102, 080601 (2009).
9. D. Zhu, M.J. Tudor, and S.P. Beeby, *Meas. Sci. Technol.* 21, 1 (2010).
10. S.C. Stanton, C.C. McGehee, and B.P. Mann, *Phys. D* 239, 640 (2010).
11. Y. Uzun and E. Kurt, *Sens. Actuator A Phys.* 192, 58 (2013).
12. Y. Uzun, E. Kurt, and H.H. Kurt, *Sens. Actuator A Phys.* 224, 119 (2015).
13. J. Qiu, J.H. Lang, and A.H. Slocum, *IEEE J. Microelectromech. Syst.* 13, 137 (2004).
14. E. Kurt, R. Kasap, and S. Acar, *Math. Comput. Appl. J.* 9, 275 (2004).
15. E. Kurt, *Nonlinear Dyn.* 45, 171 (2006).
16. S.M. Shahruz, *J. Comput. Nonlinear Dyn.* 3, 041001 (2008).
17. J.T. Lin, B. Lee, and B. Alphenaar, *Smart Mater. Struct.* 19, 1 (2010).
18. S. Roundy and P.K. Wright, *Smart Mater. Struct.* 13, 1131 (2004).
19. L. Wang and F.G. Yuan, *Smart Mater. Struct.* 045009, 17 (2008).
20. Y. Uzun and E. Kurt, in *Proceedings of 3rd International Conference on Nuclear and Renewable Energy Resources* (2012).
21. E. Kurt and Y. Uzun, in *Proceedings of 2nd International Conference on Nuclear and Renewable Energy Research* (2010).
22. Y. Uzun and E. Kurt, *Energy Conversat. Manag.* 72, 156 (2013).